Setting the Scales of the Ocean Response to Isolated Convection*

DAVID C. CHAPMAN

Woods Hole Oceanographic Institution, Woods Hole, Massachusetts

(Manuscript received 22 January 1997, in final form 15 July 1997)

ABSTRACT

The ocean response to negative buoyancy flux, applied in an isolated region at the surface, is investigated to determine the scales of the equilibrium state, that is, the time to reach equilibrium, the equilibrium density anomaly within the convecting chimney, and, in the case of deep convection, the equilibrium depth of the chimney. Two types of isolated convection, with fundamentally different parameter dependencies, are distinguished based on the importance of the forcing decay region; a region surrounding the isolated forcing region, across which the buoyancy flux decreases to zero. A narrow forcing decay region produces ''internally constrained'' convection in which the baroclinic Rossby radius is the dominant horizontal length scale, and the resulting equilibrium scales are those found by Visbeck et al. A wide forcing decay region produces ''externally constrained'' convection in which the forcing decay width is the dominant horizontal length scale, and the equilibrium scales are those found by Chapman and Gawarkiewicz.

Some simple theoretical ideas are presented that provide an estimate of the transition between the two types of convection, given by

$$\frac{W}{r_0} \approx 3.2\left(\frac{B_0}{f^3 r_0^2}\right)^{1/3} = 3.2\left(\frac{l_{\rm rot}}{r_0}\right)^{2/3},$$

where W is the width of the forcing decay region, B_0 is the surface buoyancy flux, r_0 is the radius of the forcing region, f is the Coriolis parameter, and $l_{\rm rot} = (B_0/f^3)^{1/2}$. If W is less (greater) than $3.2(l_{\rm rot}/r_0)^{2/3}$, then internally (externally) constrained convection results. This estimate is obtained for both shallow convection in which the chimney reaches the bottom almost immediately and deep convection in which the chimney never reaches the bottom. Furthermore, the transition is independent of the ambient stratification and the total water depth.

Calculations made with a primitive equation numerical model support the theoretical ideas and show that the transition between the two types of convection is smooth and well behaved. The results suggest that the forcing decay region may be important in ocean convection situations, especially for large forcing regions.

1. Introduction

Atmospheric cooling and/or brine rejection accompanying ice formation can produce negative buoyancy fluxes (i.e., buoyancy loss) in localized regions at the ocean surface. Within such regions, near-surface waters become denser and sink in narrow convective plumes, which collectively are referred to as a chimney. Dense water formed in chimneys is thought to be an important source of deep and intermediate water masses in many locations, such as the Weddell, Western Mediterranean, Labrador, and Greenland–Ice–Norwegian Seas. Furthermore, dense water formed on Arctic shelves (e.g., in coastal polynyas) appears to be largely responsible for maintaining the upper halocline of the deep Arctic basins. Clearly, understanding the dynamics of the ocean response to localized surface buoyancy forcing has important implications for global ocean circulation and climate.

Recently numerous numerical and laboratory modeling studies have focused on the dynamics of ocean convection (e.g., Brickman 1995; Coates et al. 1995; Gawarkiewicz and Chapman 1995; Jones and Marshall 1993; Maxworthy and Narimousa 1994; Whitehead et al. 1996; and numerous others). Typically, the approach is to apply a negative buoyancy flux at the model surface (or equivalently, in some laboratory models, a positive buoyancy flux at the bottom) within a limited region (usually a circular disk) to represent either localized preconditioning of the water column by, for example, topographic effects, or localized brine rejection in a coastal polynya. Qualitatively, the response in nearly all cases is as follows. A dense-water chimney penetrates downward beneath the buoyancy forcing, creating a density front along the outer edge of the chimney, between the chimney and the ambient fluid. The front adjusts toward geostrophy within one or two rotation periods, generating a vertically sheared horizontal current

* Woods Hole Oceanographic Institution Contribution Number 9408.

Corresponding author address: Dr. David C. Chapman, Physical Oceanography, Woods Hole Oceanographic Institution, Woods Hole, MA 02543.
E-mail: dchapman@whoi.edu

flowing around the rim of the chimney. If the buoyancy flux continues, the water density within the chimney increases, the chimney deepens (perhaps reaching the bottom), the front strengthens, and the rim current accelerates until baroclinic instability causes unstable waves to grow along the rim current. The waves continue to grow and, then, develop into eddies, which break up the front and exchange chimney fluid with ambient fluid. Eventually, an equilibrium is reached in which the eddy exchange is sufficient to balance the buoyancy flux through the surface. At this point, the chimney stops deepening and the density within the chimney stops increasing.

Obviously, the details of the response are highly complicated and vary from one situation or model to another. Nevertheless, and quite remarkably, Visbeck et al. (1996, hereinafter referred to as VMJ) have shown that the gross features of virtually all reported model results, whether numerical or laboratory, can be represented using a conceptually simple approach. By explicitly assuming a balance between the applied surface buoyancy flux and the lateral buoyancy flux produced by the baroclinic eddies, VMJ developed scales for (i) the maximum chimney penetration depth, (ii) the equilibrium density anomaly within the chimney, and (iii) the time to reach equilibrium, all based solely on known parameters. (Details of the VMJ scales are presented in section 2.) The scales were shown to be consistent with results from a number of different models and over a wide range of parameters, thereby dramatically improving our understanding of ocean convection and dense water formation.

All of the examples considered by VMJ used a buoyancy forcing that is spatially uniform over the entire forcing region and vanishes outside the forcing region; that is, the buoyancy flux is discontinuous at the edge of the forcing region. Recently, Chapman and Gawarkiewicz (1997, hereinafter referred to as CG) used the VMJ approach to investigate the effects of a forcing decay region, that is, a region of finite width surrounding the uniform forcing region across which the buoyancy flux decreases smoothly from its value inside the forcing region to zero. The forcing decay region is intended to represent spatial variations in the strength of atmospheric cooling or ice concentration and introduces a new horizontal length scale into the VMJ formulation. CG showed that, if the forcing decay region is wider than the baroclinic Rossby radius, then the velocity scale of the rim current is set by the width of the forcing decay region and the resulting scales are quite different from those found by VMJ. In fact, the scales involve some different parameters and are raised to different powers.

At this point, it is unclear how the two sets of scales should be reconciled and which scales should be applied in a given situation. For example, one expects that the VMJ scales should apply when the forcing decay region is narrow enough. However, the CG scales do not asymptotically approach the VMJ scales in the limit of a vanishing forcing decay region. On the other hand, the VMJ scales can be recovered by replacing the forcing decay width in the CG scales with the baroclinic Rossby radius. Are the two sets of scales consistent? Can they be reconciled in a simple way? If so, how wide must the forcing decay region be in order to set the scales? Where is the transition in parameter space?

In order to address these issues, some theoretical ideas are presented in section 2 that provide a framework for understanding the relationship between the VMJ and CG scales. I consider isolated convection, that is, away from coastlines, but the ideas are easily transferred to coastal regions, such as coastal polynyas. The theoretical ideas are developed for both ''shallow'' convection in which the chimney quickly reaches the bottom and ''deep'' convection in which the chimney never reaches the bottom. I then use a primitive equation numerical model to test the theoretical ideas for both shallow and deep convection by examining the ocean response to idealized negative buoyancy forcing (section 3). Some implications of the results are discussed in section 4, followed by some conclusions in section 5.

2. Theoretical ideas

The approach of VMJ is to assume that an equilibrium state is achieved in which the imposed surface buoyancy loss is balanced by the lateral eddy flux of buoyancy through the sides of the convective chimney. If the surface buoyancy flux B is imposed over some finite region A, then the equilibrium balance may be written as

$$\int\int \frac{\rho_0}{g} B \, dA = \int_{-h}^{0} \oint \overline{v\rho} \, dl \, dz, \tag{1}$$

where h is the chimney depth, v represents horizontal velocity fluctuations normal to the edge of the forcing region, ρ is the density anomaly relative to a constant reference density ρ_0, g is gravitational acceleration, l is distance along the perimeter of the forcing region, and z is the vertical coordinate. The overbar denotes a time average. As written, B can vary in the horizontal, and (1) could, in principle, be applied to any finite forcing region.

To proceed, I consider an isolated circular forcing region with uniform buoyancy flux B_0 within radial distance r_0, surrounded by a forcing decay region with width W across which the buoyancy flux decreases linearly from B_0 to zero (Fig. 1). The surface buoyancy flux is

$$B = \begin{cases} B_0, & r < r_0 \\ B_0(r_0 + W - r)/W, & r_0 < r < r_0 + W \\ 0, & r > r_0 + W, \end{cases} \tag{2}$$

where r is the radial distance from the center of the forcing region. Following VMJ, the eddy flux is assumed to be uniformly distributed over the sides of the chimney and proportional to $v\rho$, with proportionality constant α that accounts for the imperfect correlation

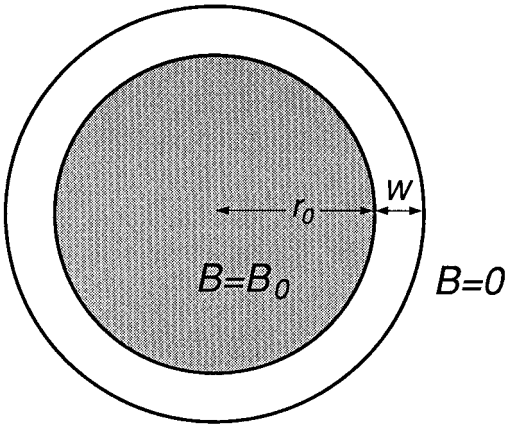

FIG. 1. Plan view of the forcing region: a constant buoyancy flux B_0 is applied over a circular region of radius r_0 and decreases linearly to zero across the forcing decay region of width W.

between v and ρ and any spatial variability of the eddy flux; that is, $\overline{v\rho} \approx \alpha v\rho$. For simplicity (following CG), the buoyancy flux within the forcing decay region is ignored (see the appendix for formal justification), so (1) may be approximated by

$$\left(\frac{1}{2\alpha}\right)\frac{\rho_0}{g}B_0 r_0 = hv\rho. \tag{3}$$

Estimates of h, v, and ρ are used in (3) to produce either the VMJ or the CG scales. At this point, the coefficient α is unknown and can be found empirically from laboratory and numerical model results.

The depth of convective penetration is estimated by the one-dimensional deepening of a mixed layer

$$h = \frac{(2Bt)^{1/2}}{N}, \tag{4}$$

where t is time, and N is the initial buoyancy frequency of the ambient fluid, taken here to be constant. If the fluid is so weakly stratified that the mixed layer depth quickly reaches the total fluid depth H, then h in (3) is replaced by H and the background stratification can be ignored (Fig. 2a). The density front around the edge of the forcing region extends from surface to bottom, and this is called shallow convection. If N is large enough that $h < H$ in the equilibrium state, then h is approximated by (4) (Fig. 2b); this is called deep convection. Intermediate cases in which $h \to H$ as equilibrium is approached are not considered here.

The estimate of the velocity v distinguishes the VMJ and CG scales. In both cases, the velocity in the eddies should scale like the velocity along the rim current at the onset of instability, when the rim current velocity v_g is nearly geostrophic and can be estimated from the thermal wind balance

$$\frac{\partial v_g}{\partial z} = -\frac{g}{\rho_0 f}\frac{\partial \rho}{\partial r}, \tag{5}$$

where f is the Coriolis parameter. The velocity v is then set equal to v_g at the surface; that is, $v = v_g(z = 0)$. Equation (5) requires estimates of both the vertical shear and the horizontal density gradient. The vertical shear estimate depends on whether the convection is shallow or deep, but it does not involve the forcing decay width W and so does not determine which set of scales results. Rather it is the length scale used to approximate the horizontal density gradient that determines which scales, VMJ or CG, are obtained. If the estimate of the horizontal density gradient is based on the baroclinic Rossby radius associated with the density front along the edge of the forcing region R_d, then the VMJ scales result. If the estimate of the horizontal density gradient is based on the width of the forcing decay region W, then the CG scales result. But, under what conditions is each of these scales appropriate?

One way to decide which horizontal scale is appropriate is to consider the time development of the rim current velocity and the baroclinic Rossby radius. Both v_g and R_d are initially zero because there is no horizontal density gradient. Immediately after the buoyancy flux is imposed, a small horizontal density gradient is established over the width W, but R_d remains small because it is proportional to the total density difference across the frontal region. Thus, $R_d \ll W$ in the early stages of convection, and the velocity in (5) should be set by W. As time progresses, the density difference across the front increases, so R_d increases whereas W remains fixed (Figs. 2a,b). In the absence of horizontal motions, the density difference across the front will eventually increase to the point where R_d surpasses W. The fluid should then respond on the scale R_d, so R_d would set the velocity in (5). However, at some time during the full three-dimensional development, the front becomes unstable, breaks up into eddies, and reaches the equilibrium balance (1). If this occurs while R_d is small and W is setting v_g, then the CG scales should apply. I call this *externally constrained convection* because the response is constrained by the forcing decay width that is externally imposed on the fluid. If the frontal breakup occurs after R_d has increased enough to set v_g, then the VMJ scales should apply. I call this *internally constrained convection* because the response is basically constrained by the internal properties of the fluid. Note that, in the absence of a forcing decay region (i.e., $W = 0$), the above reasoning implies that R_d always sets the velocity, so the convection is internally constrained and the VMJ scales apply. This is reassuring because the VMJ scales are based on cases with $W = 0$. These ideas are formalized below for both shallow and deep convection.

a. Shallow convection

In shallow convection, the effects of ambient stratification are negligible, so the fluid may be assumed initially homogeneous (i.e., $N = 0$). The chimney reach-

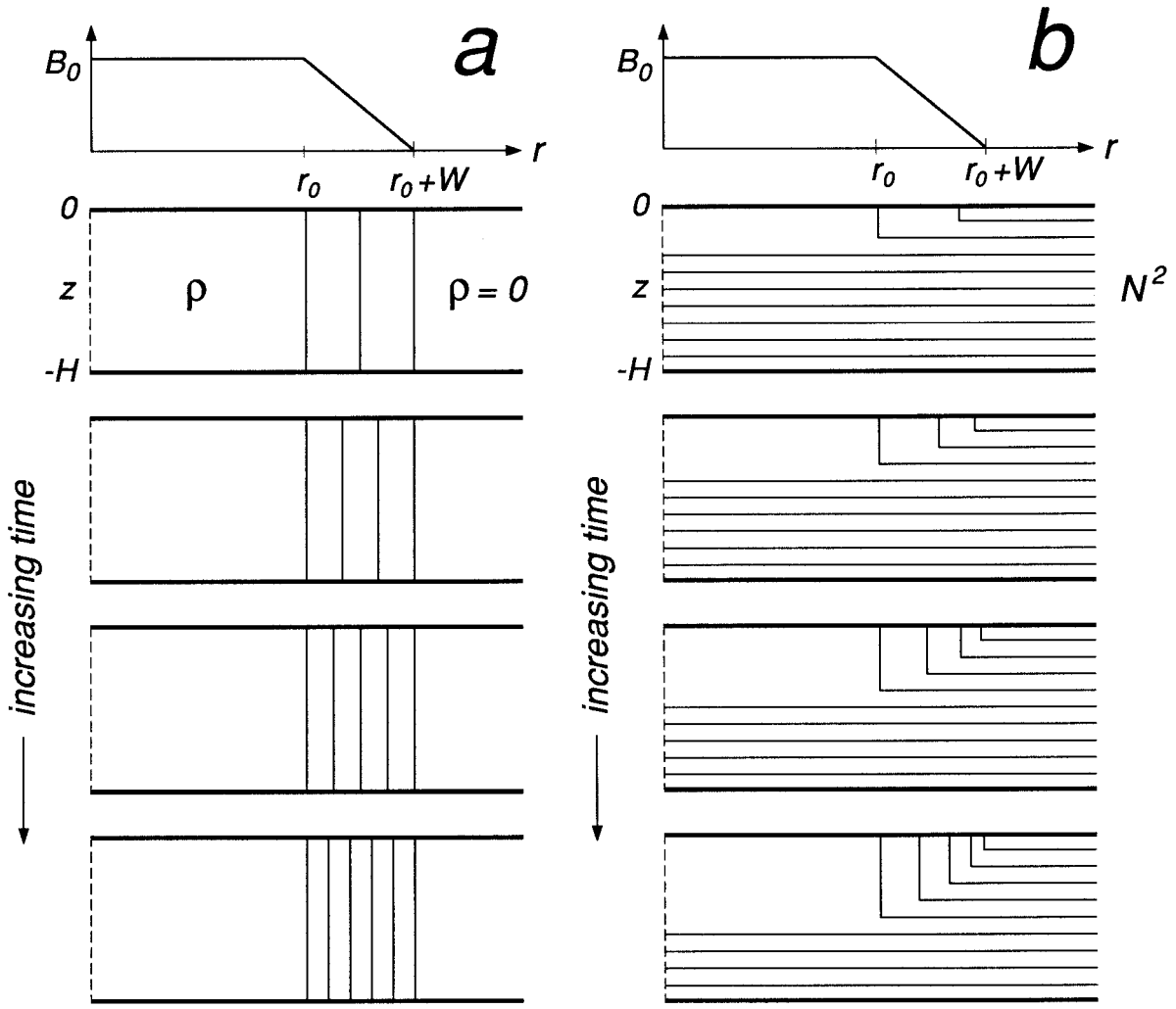

FIG. 2. Schematic of the vertical structure of the density field during its initial development for (a) shallow and (b) deep convection, based solely on one-dimensional vertical mixing. The left boundary represents the center of the forcing region. A density front forms beneath the forcing decay region ($r_0 < r < r_0 + W$). The density gradient increases with time, as does the chimney depth for deep convection.

es the bottom rapidly ($h = H$), establishing a surface-to-bottom density front around the forcing region (Fig. 2a). In the absence of bottom friction, the velocity along the rim current is nearly antisymmetric with depth; that is, the cyclonic current at the surface is nearly equal and opposite to the anticyclonic current at the bottom so that the vertical shear can be approximated by $\partial v_g/\partial z \approx 2v/H$. The density anomaly beneath the uniform forcing region (i.e., $r < r_0$) increases linearly with time,

$$\rho = \frac{\rho_0 B_0}{gH} t. \tag{6}$$

The baroclinic Rossby radius is defined as

$$R_d = \frac{(\rho g H/\rho_0)^{1/2}}{f}. \tag{7}$$

For externally constrained convection, $\partial\rho/\partial r \approx -\rho/W$. Using the above approximations and (6), the velocity is estimated from (5) as

$$v_{se} \approx \frac{B_0}{2fW} t, \tag{8}$$

where the subscript indicates shallow, externally constrained convection. Substituting (6) and (8) into (3) yields an estimate of the time to reach equilibrium

$$t_{se} = \left(\frac{1}{\alpha}\right)^{1/2} \left(\frac{f r_0 W}{B_0}\right)^{1/2}. \tag{9}$$

Combining (6) and (9) produces an estimate of the equilibrium density anomaly

$$\rho_{se} = \left(\frac{1}{\alpha}\right)^{1/2} \frac{\rho_0}{gH} (f B_0 r_0 W)^{1/2}. \tag{10}$$

These are the same scales found by CG when applied to a semicircular forcing region.

For internally constrained convection, the vertical shear is again $\partial v_g/\partial z \approx 2v/H$, while $\partial\rho/\partial r \approx -\rho/R_d$ with R_d given by (7). The velocity estimate from (5) is now

$$v_{si} \approx \frac{1}{2}(B_0 t)^{1/2}, \tag{11}$$

where the subscript indicates shallow, internally constrained convection. Using (11) with (6) in (3), the equilibrium time and equilibrium density anomaly become

$$t_{si} = \left(\frac{1}{\alpha}\right)^{2/3}\left(\frac{r_0^2}{B_0}\right)^{1/3}; \qquad \rho_{si} = \left(\frac{1}{\alpha}\right)^{2/3}\frac{\rho_0}{gH}(B_0 r_0)^{2/3}. \tag{12}$$

These are the scales found by VMJ for shallow convection (with their α' replaced by $\alpha/2$).

As argued above, the velocity should initially follow v_{se} because R_d is initially small. The transition to internally constrained velocity occurs when $v_{se} = v_{si}$, which takes place at

$$t_s^* = \frac{f^2 W^2}{B_0}. \tag{13}$$

If the equilibrium is reached before the transition, that is, $t_{se} < t_s^*$, then the forcing decay width must have set the velocity, so (9) and (10) must apply. If the transition occurs before the equilibrium is reached, that is, $t_s^* < t_{se}$, then the Rossby radius will have set the velocity, so (12) must apply. Of course, the transition is expected to be smooth and not abrupt, so there must be some range of intermediate cases for which neither set of scales applies precisely. Calculations presented in section 3 confirm this.

The transition occurs when $t_{se} = t_s^*$, that is, when

$$\frac{W}{r_0} = \left(\frac{1}{\alpha}\right)^{1/3}\left(\frac{B_0}{f^3 r_0^2}\right)^{1/3} = \left(\frac{1}{\alpha}\right)^{1/3}\left(\frac{l_{rot}}{r_0}\right)^{2/3}, \tag{14}$$

where $l_{rot} = (B_0/f^3)^{1/2}$ is the vertical length scale over which rotation becomes important in the sinking process (see Jones and Marshall 1993). Given α, f, B_0, and r_0, the convection is externally constrained when $W/r_0 > (1/\alpha)^{1/3}(l_{rot}/r_0)^{2/3}$, while it is internally constrained when $W/r_0 < (1/\alpha)^{1/3}/(l_{rot}/r_0)^{2/3}$. It is interesting to note that (14) is independent of H, so it applies to any total water depth, provided that the stratification is weak enough that shallow convection is realized. The implications of (14) are discussed in section 4.

Strictly speaking, the transition time t_s^* should be compared with the time at which the eddies grow to finite amplitude because this is when the eddy velocity is actually set. Equilibrium is reached only after the eddies have had time to exchange dense and ambient waters, that is, the third (eddy transport) stage described by Gawarkiewicz and Chapman (1995). However, the delay is not long and the precise time when the eddy velocity is set is difficult to determine, so a comparison with the equilibrium time t_{se} is used here. As a result, (14) predicts a transition at a slightly larger W than found in the numerical calculations.

Finally, I note that the above development is unchanged when applied to a semicircular coastal polynya, as in CG (with their $a = b = r_0$). More generally, it can be extended to isolated ellipses or half-elliptical coastal polynyas by changing the area and perimeter formulas, which changes only the coefficients involving α, as in CG.

b. Deep convection

In deep convection, the stratification is strong enough that the chimney never penetrates to the bottom (Fig. 2b). The surface mixed layer grows beneath the forcing decay region with depth given locally by (4). The density anomaly at the surface is equal to the ambient density anomaly at depth h, given by

$$\rho = \rho_0 N^2 h/g. \tag{15}$$

The baroclinic Rossby radius is defined as

$$R_d = Nh/f. \tag{16}$$

For externally constrained convection, the vertical shear in the rim current may be approximated by $\partial v_g/\partial z \approx 2v/h$. The horizontal density gradient in the frontal region (i.e., $r_0 < r < r_0 + W$) is estimated by combining (2), (4), and (15) to obtain

$$\frac{\partial\rho}{\partial r} \approx \frac{\rho_0 N^2}{g}\frac{\partial h}{\partial r} = -\frac{\rho_0 B_0}{gWh}t.$$

Substituting these approximations into (5) yields

$$v_{de} \approx \frac{B_0}{2fW}t, \tag{17}$$

where the subscript indicates deep, externally constrained convection. Equilibrium is reached when the center of the chimney reaches the equilibrium depth. This time is estimated by substituting (15) and (17) into (3) and then using (4), evaluated at the center of the chimney where $B = B_0$, to obtain

$$t_{de} = \left(\frac{1}{2\alpha}\right)^{1/2}\left(\frac{f r_0 W}{B_0}\right)^{1/2}. \tag{18}$$

Substituting (18) into (4) and the result into (15) produces estimates of both the density anomaly and chimney depth at equilibrium:

$$\rho_{de} = \left(\frac{2}{\alpha}\right)^{1/4}\frac{\rho_0 N}{g}(f B_0 r_0 W)^{1/4};$$

$$h_{de} = \left(\frac{2}{\alpha}\right)^{1/4}\frac{1}{N}(f B_0 r_0 W)^{1/4}. \tag{19}$$

These estimates were also obtained by CG.

For internally constrained convection, the velocity

may be estimated following Jones and Marshall (1997) as follows. The horizontal density gradient in the frontal region is estimated as $\partial\rho/\partial r \approx -\rho/R_d$ where R_d is given by (16). The density difference across the front varies linearly with depth as

$$\rho = \frac{\rho_0 N^2}{g} h\left(1 + \frac{z}{h}\right). \tag{20}$$

Substituting into (5) and integrating vertically yields

$$v_g \approx Nh\left(\frac{z^2}{2h^2} + \frac{z}{h} + \frac{1}{3}\right), \tag{21}$$

where the constant of integration has been chosen to make the depth integral of v_g (from $-h$ to 0) vanish. From (21), the surface velocity estimate is

$$v_{\rm di} \approx \frac{\sqrt{2}}{3}(B_0 t)^{1/2}, \tag{22}$$

where the subscript indicates deep, internally constrained convection. Combining (4), evaluated at the chimney center where $B = B_0$, with (15) and (22) yields the equilibrium time, density anomaly, and chimney depth:

$$t_{\rm di} = \frac{1}{2}\left(\frac{3}{2\alpha}\right)^{2/3}\left(\frac{r_0^2}{B_0}\right)^{1/3}; \qquad \rho_{\rm di} = \left(\frac{3}{2\alpha}\right)^{1/3}\frac{\rho_0 N}{g}(B_0 r_0)^{1/3};$$

$$h_{\rm di} = \left(\frac{3}{2\alpha}\right)^{1/3}\frac{1}{N}(B_0 r_0)^{1/3}. \tag{23}$$

These are the VMJ scales for deep convection (with their α' replaced by $\alpha/3$).

The transition from externally constrained convection to internally constrained convection occurs when $v_{\rm de} = v_{\rm di}$ at

$$t_d^* = \frac{8}{9}\frac{f^2 W^2}{B_0}. \tag{24}$$

If equilibrium is reached before the transition, that is, $t_{\rm de} < t_d^*$, then (18) and (19) must apply. If the transition occurs before equilibrium, that is, $t_d^* < t_{\rm de}$, then (23) applies. The transition occurs when $t_{\rm de} = t_d^*$, that is, when

$$\frac{W}{r_0} = \left(\frac{9}{8}\right)^{2/3}\left(\frac{1}{2\alpha}\right)^{1/3}\left(\frac{B_0}{f^3 r_0^2}\right)^{1/3} = \left(\frac{9}{8}\right)^{2/3}\left(\frac{1}{2\alpha}\right)^{1/3}\left(\frac{l_{\rm rot}}{r_0}\right)^{2/3}. \tag{25}$$

Given α, f, B_0, and r_0, the convection is externally constrained when $W/r_0 > (9/8)^{2/3}(1/2\alpha)^{1/3}(l_{\rm rot}/r_0)^{2/3}$, while it is internally constrained when $W/r_0 < (9/8)^{2/3}(1/2\alpha)^{1/3}(l_{\rm rot}/r_0)^{2/3}$. Note that (25) is independent of both H and N. Thus, neither the total depth nor the ambient stratification influences whether the forcing decay width or the baroclinic Rossby radius sets the scales for convection. Also note the similarities between shallow and deep convection; $v_{\rm se} = v_{\rm de}$, $v_{\rm si} \approx v_{\rm di}$, $t_s^* \approx t_d^*$ and the only substantial difference between (14) and (25) is the factor of 2 multiplying α.

3. Numerical tests

a. Model description

The theoretical ideas presented above are tested here using the semispectral primitive equation model (SPEM) developed by Haidvogel et al. (1991) to solve the following hydrostatic and Boussinesq momentum, density, and continuity equations:

$$\mathbf{u}_t + (\mathbf{u}\cdot\nabla)\mathbf{u} + w\mathbf{u}_z + f(\mathbf{k}\times\mathbf{u}) = -\frac{1}{\rho_0}\nabla p + (A_V\mathbf{u}_z)_z + F_u \tag{26}$$

$$p_z = -\rho g \tag{27}$$

$$\rho_t + (\mathbf{u}\cdot\nabla)\rho + w\rho_z = (K_V\rho_z)_z + F_\rho \tag{28}$$

$$\nabla\cdot\mathbf{u} + w_z = 0. \tag{29}$$

In this system $\mathbf{u}$, w represent the horizontal and vertical (z) components of the velocity, p is the pressure, A_V is the vertical eddy viscosity, K_V is the vertical eddy diffusivity, $\mathbf{k}$ is the vertical unit vector, $\nabla = (\partial/\partial x, \partial/\partial y)$ is the horizontal gradient operator, and ρ, ρ_0, f, g, and t have been previously defined. The variables $F_{u,\rho}$ represent dissipative functions that are required for numerical stability. Subscripts z and t denote partial differentiation.

Two versions of SPEM are used. An older version (SPEM3.0) is used for the shallow convection calculations (section 3a), while a newer version (SPEM5.1) is used for the deep convection calculations (section 3b). In both cases, the system (26)–(29) is approximated by finite differences in the horizontal, and a leapfrog-trapezoidal time stepping scheme is used with an occasional trapezoidal step correction. The primary difference for the present calculations is the representation of vertical structure. SPEM3.0 uses a high-order spectral approximation (an expansion in modified Chebyshev polynomials), while SPEM5.1 uses finite differences. SPEM3.0 can produce spurious high mode amplitudes in deep convection calculations (e.g., Alverson 1995), while SPEM5.1 produces a well-behaved response. Furthermore, SPEM3.0 restricts the vertical grid points to be at the extrema of the Chebyshev polynomials, which occur near the surface and bottom boundaries, while SPEM5.1 allows nearly arbitrary placement of vertical grid points, a desireable feature for representing chimneys that do not reach the bottom. The limitations of SPEM3.0 are not a factor in shallow convection because the dense fluid mixes to the bottom immediately. Several shallow convection calculations have been repeated using SPEM5.1 with nearly identical results.

The model domain is a high-latitude, uniformly rotating ($f = 1.3 \times 10^{-4}\ {\rm s}^{-1}$), straight channel with walls

at $y = -50$ and 50 km and periodic open boundaries at $x = -50$ and 50 km. The channel is wide enough and long enough that the boundaries do not significantly influence the evolution of the dynamics during the time of interest here. The ocean has constant depth, with no flow through the bottom and a rigid lid at the surface (i.e., $w = 0$ at $z = 0$). The numerical grid is uniform in the horizontal with 96 grid cells in each direction (i.e., $\Delta x = \Delta y = 1.04$ km). Additional calculations with higher resolution have been made for small W, which confirm that the results are not sensitive to the grid size. For the shallow convection calculations, nine polynomials are used to resolve the full depth ($H = 50$ m), and the time step is 288 s. For the deep convection calculations, 30 vertical grid cells are used to resolve the full depth ($H = 2000$ m), with spacing varying smoothly from a minimum of 42 m at the surface to 163 m at the bottom, and the time step is 432 s.

Both surface and bottom stresses are set to zero: $A_V \mathbf{u}_z = 0$ at $z = 0, -H$. Buoyancy forcing is applied by setting $K_V \rho_z = \rho_0 B/g$ at the surface, where B is given by (2) and is centered at $x = y = 0$ (i.e., $r^2 = x^2 + y^2$). There is no density flux through the bottom: $K_V \rho_z = 0$ at $z = -H$. As in CG, the vertical mixing coefficients are specified using a Richardson-number-dependent scheme:

$$A_V = 0.0001 + \frac{0.0049}{(1. + 0.3\mathrm{Ri})^{1/2}} \tag{30}$$

$$K_V = 0.0001 + \frac{0.0049}{(1. + 0.3\mathrm{Ri})^{3/2}}, \tag{31}$$

where the units are $m^2\ s^{-1}$ and the Richardson number is defined by

$$\mathrm{Ri} = \frac{-g\rho_z/\rho_0}{|\mathbf{u}_z|^2}. \tag{32}$$

Additional vertical mixing of density is applied in the form of instantaneous vertical convective adjustment whenever the water column becomes statically unstable (i.e., when lighter water appears under heavier water). Lateral diffusion of both momentum and density is necessary for numerical stability. I apply Laplacian subgrid-scale mixing with constant mixing coefficients (i.e., $F_u = \nu_u \nabla^2 \mathbf{u}$; $F_\rho = \nu_\rho \nabla^2 \rho$) while using small mixing coefficients, $\nu_u = 25\ m^2\ s^{-1}$ and $\nu_\rho = 5\ m^2\ s^{-1}$.

Each calculation begins from rest, with the surface buoyancy flux applied at $t = 0$ and held constant for the duration of the calculation. Calculations are halted when eddies reach the model boundaries. The exchange of chimney water with ambient water by eddies is diagnosed by recording the average density anomaly at the surface in a small area at the center of the forcing region. Typically, the density anomaly there follows the one-dimensional increase, given by (6) or by (15) combined with (4), until eddies reach the center, after which the density anomaly fluctuates about a fairly constant value (see CG for examples). The actual equilibrium density anomaly is only slightly different from the density anomaly at which the response breaks away from the one-dimensional increase. Therefore, in the interest of computational efficiency, the equilibrium density anomaly in this paper is taken to be the first maximum density anomaly after the response breaks away from the one-dimensional increase. This allows shorter calculations in a smaller domain, while changing the estimates of α by no more than 10%–15%, given the 2/3 and 1/2 powers in the scales. This error is well within the range of uncertainty in the estimates of α based on longer calculations (see CG and VMJ). The important point is that the estimates are made consistently from one case to the next.

b. Shallow convection

A series of shallow convection calculations has been made to test the theoretical ideas developed in section 2. For all calculations, the depth, Coriolis parameter, forcing region radius, and buoyancy flux are fixed at $H = 50$ m, $f = 1.3 \times 10^{-4}\ s^{-1}$, $r_0 = 20$ km, and $B_0 = 16.9 \times 10^{-7}\ m^2\ s^{-3}$. The response for other combinations has been examined, but these values are convenient because they allow testing of the theoretical ideas using a sensible range of forcing decay widths, $2 \le W \le 10$ km, while still spanning the transition from internally to externally constrained convection. The parameter choices are all reasonable except perhaps the buoyancy flux, which is considerably larger than typical observed values. This value for B_0 was chosen to make $t_s^* = 0.5 t_{se}$ when $W = 5$ km, using $(1/\alpha)^{1/2} = 5.7$ based on CG. Smaller, more realistic buoyancy fluxes lead to a dominance of externally constrained convection for reasonable W, making it harder to examine the transition between internally and externally constrained convection.

The ocean is initially quiescent with uniform (reference) density $\rho_0 = 1000\ kg\ m^{-3}$. Typical behavior of the density front surrounding the forcing region is illustrated in Fig. 3. The smooth, circular density front shows a hint of unstable waves by day 3, then rapidly develops meanders by day 4 and eddies by day 5. This pattern is remarkably similar for all forcing decay widths W, with a mode 8 wave (wavelength of 15.7 km) always dominating. The only noticeable difference is that the unstable wave growth is delayed for larger W. These features indicate that the mode number (i.e., dominant wavelength) is determined by the density difference across the front rather than W, consistent with the findings of CG.

The simplest test of the theoretical ideas presented in section 2 is to examine the time development of the model velocity. The velocity at the surface should initially increase linearly according to (8) until $t = t_s^*$, after which the Rossby radius should take over, producing the square root dependence of (11). Using the parameter values listed above, the maximum cyclonic velocity at the surface (along $x = 0$ km) is plotted versus time for

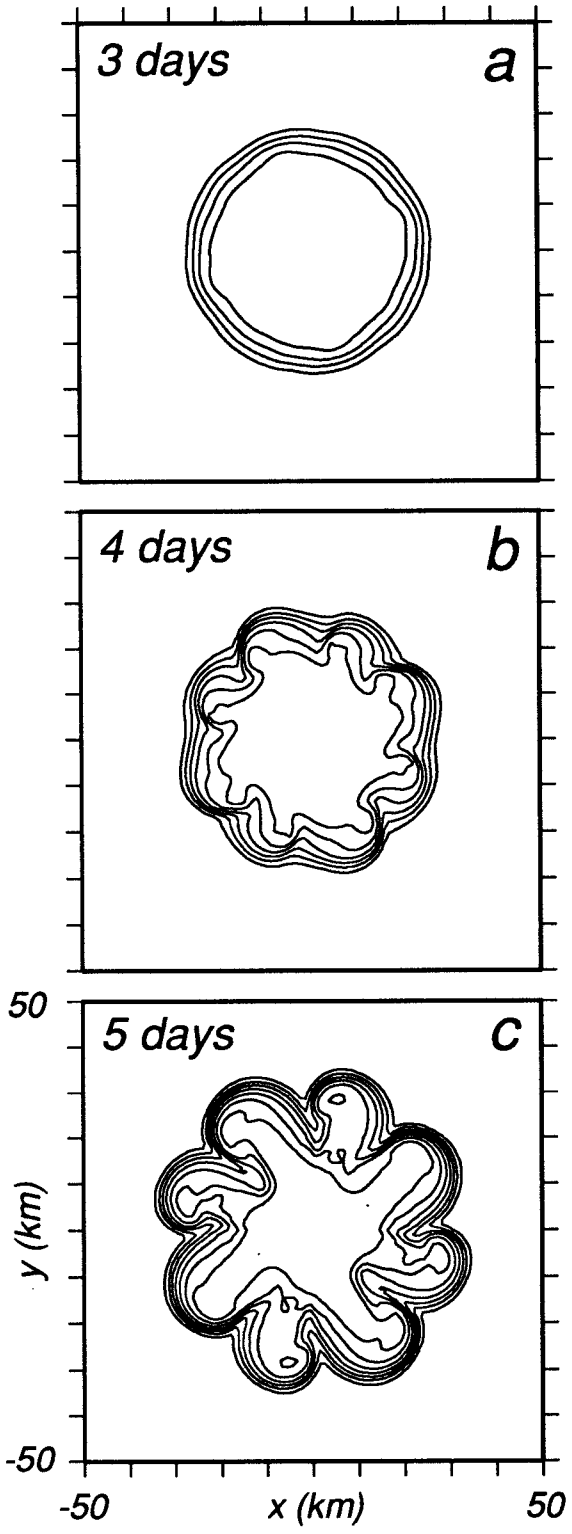

Fig. 3. Plan view of bottom density anomaly during shallow convection after 3, 4, and 5 days of forcing with $B_0 = 16.9 \times 10^{-7}$ m^2 s^{-3}, $r_0 = 20$ km, $W = 5$ km, $f = 1.3 \times 10^{-4}$ s^{-1}, and $H = 50$ m. Contour interval is 0.2 kg m^{-3}, starting with the outermost contour of 0.1 kg m^{-3}.

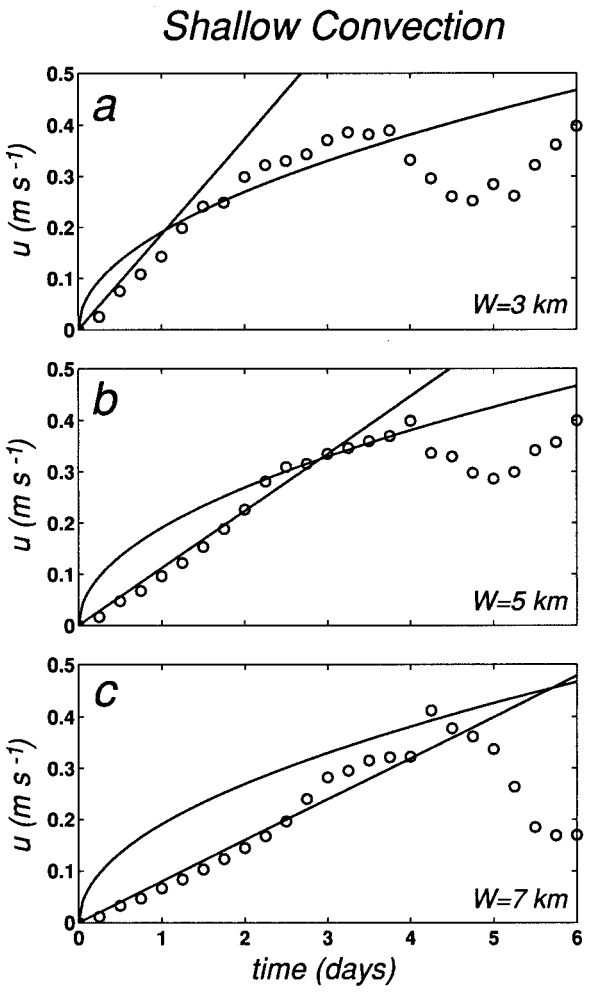

FIG. 4. Maximum cyclonic velocity at the surface within the rim current (open circles) vs time during shallow convection, with $B_0 = 16.9 \times 10^{-7}$ m^2 s^{-3}, $r_0 = 20$ km, $f = 1.3 \times 10^{-4}$ s^{-1}, $H = 50$ m, and $W =$ (a) 3, (b) 5, and (c) 7 km. The straight line corresponds to the expected velocity for externally constrained convection given by (8), while the curve corresponds to the expected velocity for internally constrained convection given by (11). The intersection of the curves occurs at t_s^*.

three choices of forcing decay width (Fig. 4). In each case, the straight line is the velocity expected from (8), the slope of which varies with W, while the curve is the velocity expected from (11). The transition time t_s^* occurs where the two curves intersect. The circles are the numerical model velocities. Clearly, the model velocity initially follows the linear curve as predicted, with some slight differences associated with the approximate nature of (8) and (11). After t_s^*, the model velocity tends to follow the square root curve as predicted until the unstable waves grow large enough to violate the theoretical assumptions, generating wildly varying velocities. There is some discrepancy in the details of the transition for $W = 5$ km and after about 2.5 days for $W = 7$ km, which is associated with cross-frontal circulation, such as the slumping of the dense

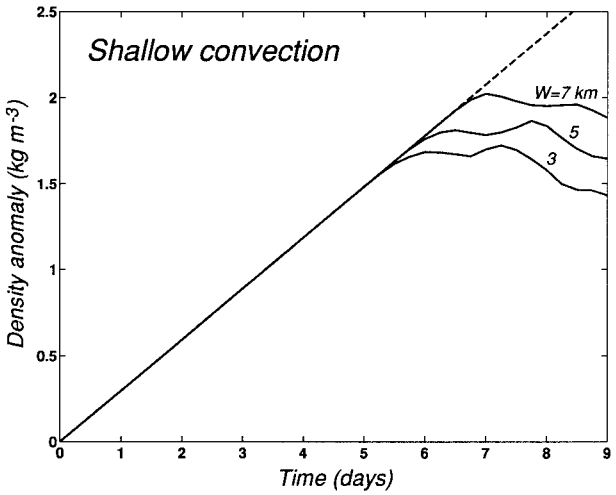

FIG. 5. Density anomaly within the forcing region vs time for the cases shown in Fig. 4. The straight dashed line is the one-dimensional response given by (6).

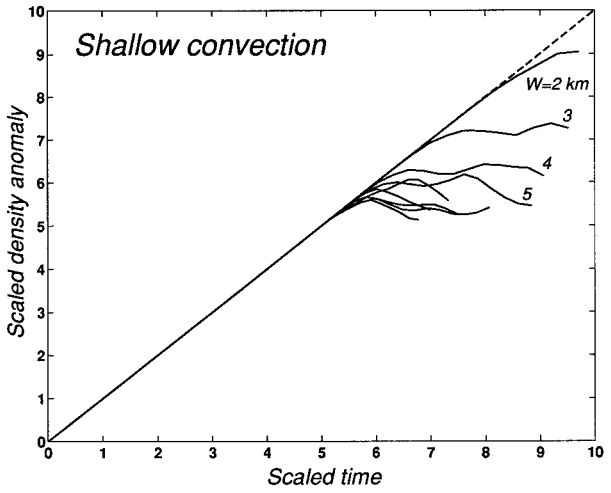

FIG. 6. Density anomaly within the forcing region vs time with both axes scaled for shallow, externally constrained convection using (9) and (10). Each curve represents the response for a different forcing decay width W from 2 to 10 km in unit increments. Only the first four curves are labeled to avoid confusion. Other parameters are $B_0 = 16.9 \times 10^{-7}$ m^2 s^{-3}, $r_0 = 20$ km, $f = 1.3 \times 10^{-4}$ s^{-1}, and $H = 50$ m.

fluid radially outward at the bottom and radially inward at the surface. This alters the velocities but is not accounted for in the approximations in section 2. Overall, the model results are supportive of the theory.

The model velocities for all cases in Fig. 4 separate rather abruptly from the theoretical curves near day 4, indicating that the eddies are breaking up the rim current. However, equilibrium is not approached until day 6 or 7 (Fig. 5) because it takes time for the eddies to exchange dense and ambient fluids and, thereby, balance the buoyancy fluxes. The velocity of the eddies is presumably set during eddy development, that is, closer to day 4 than to equilibrium. This means that the velocities (5) and (11) produce overestimates of the equilibrium velocity. This difference is taken into account by the eddy exchange efficiency α in producing the scales (9) and (10), but not in estimating the transition. The result is an overestimate of the transition from externally to internally constrained convection; that is, the transition actually occurs at a smaller W than predicted by (14).

Additional calculations were made with integer values of W from 2 to 10 km. The density anomaly for each case is plotted versus time in Fig. 6, scaled according to (9) and (10) as if the convection were externally constrained. If this scaling is correct, then the curves should overlay. The curves for small W clearly do not overlay with the others, but the curves for $W > 5$ km break away from the linear increase at nearly the same time, giving a scaled equilibrium density anomaly of $(1/\alpha)^{1/2} \approx 5.7$. (This is the same value found by CG, which confirms their contention that boundary effects are minimal in the coastal polynya case.) Thus, Fig. 6 indicates that convection is internally constrained for $W < 4$ km and externally constrained for $W > 5$ km. As expected, the transition predicted from (14) occurs at the somewhat larger value of $W = 7.9$ km.

A more striking view of the transition is shown in Fig. 7, where the unscaled equilibrium density anomaly is plotted versus W. The equilibrium density anomaly is nearly constant for small W, as it should be for internally constrained convection. The constant value of $\rho_{si} \approx 1.7$ kg m^{-3} can be used in (12) to estimate $(1/\alpha)^{2/3} \approx 8$, from which $\alpha \approx 0.044$. For $W > 5$ km, the model closely follows the theoretical curve based on (10) with $(1/\alpha)^{1/2} = 5.7$ ($\alpha \approx 0.031$), indicating

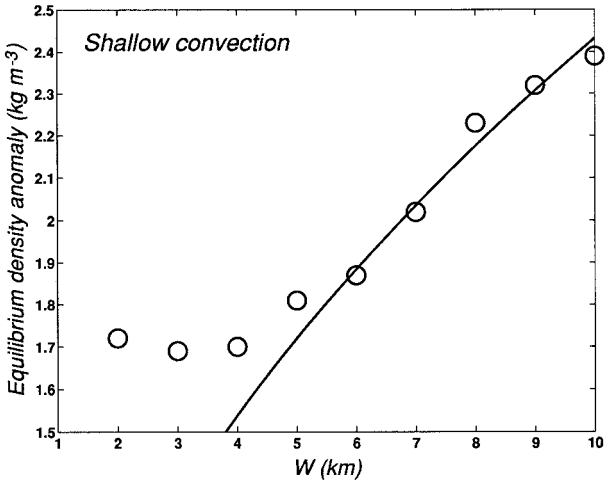

FIG. 7. Equilibrium density anomaly for various forcing decay widths (open circles) based on the shallow convection results shown in Fig. 6 (before scaling). The solid curve is the expected value for externally constrained convection given by (10) with $\alpha = 0.031$. Other parameters are $B_0 = 16.9 \times 10^{-7}$ m^2 s^{-3}, $r_0 = 20$ km, $f = 1.3 \times 10^{-4}$ s^{-1}, and $H = 50$ m. For small W, the convection should be internally constrained with equilibrium density anomaly independent of W.

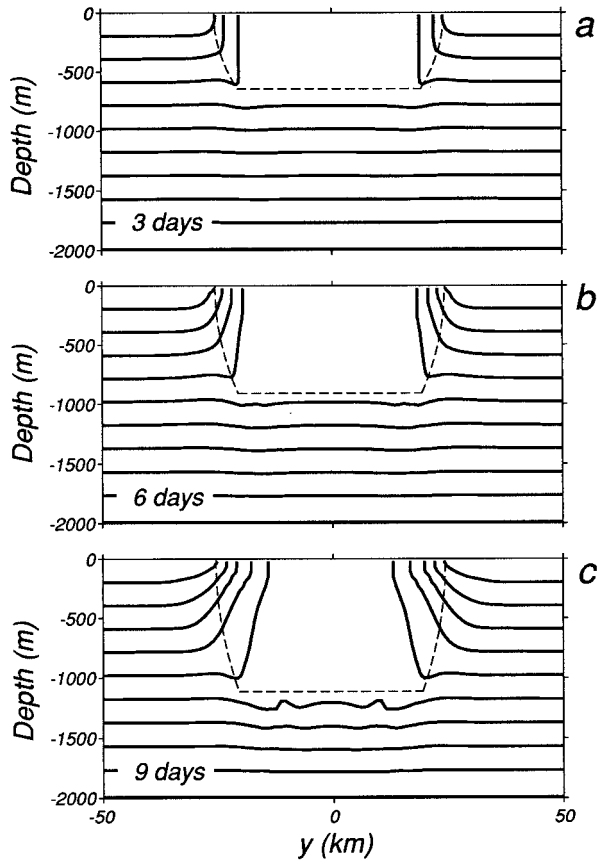

FIG. 8. Vertical section of density anomaly during deep convection after 3, 6, and 9 days of forcing with $B_0 = 8 \times 10^{-7}$ m^2 s^{-3}, $r_0 = 20$ km, $W = 5$ km, $f = 1.3 \times 10^{-4}$ s^{-1}, $N = 0.001$ s^{-1}, and $H = 2000$ m. The dashed curve in each panel shows the chimney depth based solely on one-dimensional vertical mixing given by (4).

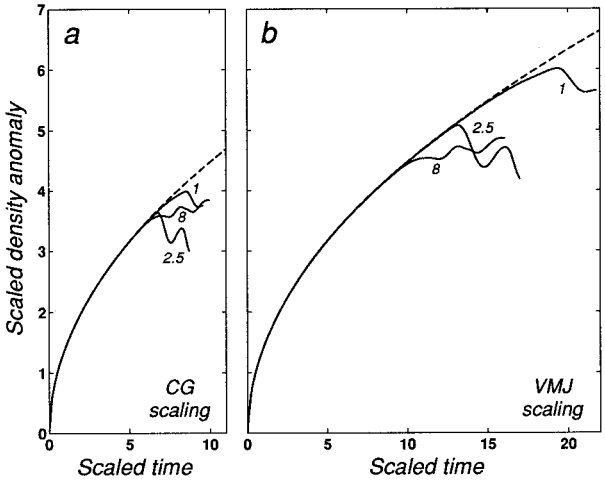

FIG. 9. Density anomaly within the forcing region versus time with both axes scaled for deep convection: (a) externally constrained using (18) and (19) and (b) internally constrained using (23). Each curve represents the response for a different buoyancy flux, $B_0 = 1$, 2.5 or 8×10^{-7} m^2 s^{-3}, with $r_0 = 20$ km, $W = 5$ km, $f = 1.3 \times 10^{-4}$ s^{-1}, $N = 0.001$ s^{-1}, and $H = 2000$ m. The dashed curve is the one-dimensional response given by (15) combined with (4).

externally constrained convection and confirming the transition at $W \approx 5$ km.

c. Deep convection

A series of numerical calculations was also made to test the theoretical ideas for deep convection. For all calculations, the depth, Coriolis parameter, and forcing region radius are fixed at $H = 2000$ m, $f = 1.3 \times 10^{-4}$ s^{-1}, and $r_0 = 20$ km. The buoyancy flux is set at $B_0 = 8 \times 10^{-7}$ m^2 s^{-3} for most calculations, but other values are also used where noted. The ocean is initially stratified with constant buoyancy frequency $N = 0.001$ s^{-1}. The forcing decay width is varied over the range $0 \leq W \leq 10$ km.

The response in all cases is qualitatively like that found in other studies of deep convection. Figure 8 shows the deepening of the chimney with time for the case of $W = 5$ km. In each panel, the expected penetration depth based on (2) and (4) is indicated by the dashed curve, showing that the chimney basically deepens according to the one-dimensional mixed layer formula.

The scalings for externally constrained deep convection, (18) and (19), have never been demonstrated with model calculations, so I first vary the buoyancy flux B_0 to establish their validity. Buoyancy fluxes of $B_0 = 1$, 2.5, and 8 ($\times 10^{-7}$ m^2 s^{-3}) are applied with $W = 5$ km, and the resulting time dependence of the density anomaly within the chimney is plotted in Fig. 9 using both the externally constrained (CG) and internally constrained (VMJ) scalings. The CG scalings collapse the results much closer to a single curve than do the VMJ scalings, suggesting that the convection is externally constrained. The curves in Fig. 9a leave the one-dimensional response at a scaled density anomaly of about $(2/\alpha)^{1/4} \approx 3.5$ from (19), producing an estimate of $\alpha \approx 0.013$. Using this value in (25), $W/r_0 > (9/8)^{2/3}(1/2\alpha)^{1/2}(l_{\rm rot}/r_0)^{2/3}$ for all three cases, confirming that they are indeed externally constrained. Of course, these three examples do not completely verify the CG scalings but they are supportive and provide enough evidence to proceed. The results below provide additional confirmation.

The importance of the forcing decay region is demonstrated, in Fig. 10, for the case of $W = 10$ km. The rim current is nearly in geostrophic balance, with the model vertical shear almost balancing the thermal wind shear [i.e., right-hand side of (5)] across the surface of the rim current after 3 days, before instabilities have developed. Also shown is the theoretical thermal wind shear (thin line), estimated solely based on the one-dimensional chimney depth (4),

$$\frac{\partial v_g}{\partial z} = -\frac{g}{\rho_0 f}\frac{\partial \rho}{\partial r} \approx \frac{N^2}{f}\frac{\partial h}{\partial r}$$

$$= \frac{N}{f}\left(\frac{B_0 t}{2W}\right)^{1/2}(r_0 + W - r)^{-1/2}, \qquad (33)$$

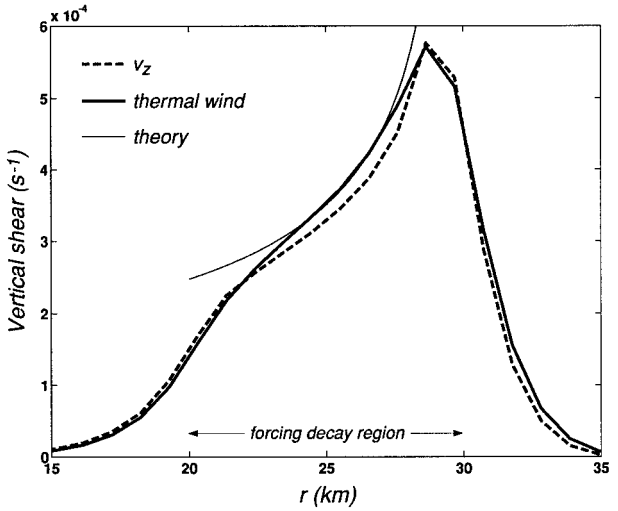

FIG. 10. Vertical shear at the surface of the rim current (20 km $< r <$ 30 km) after 3 days of deep convective forcing with $B_0 = 8 \times 10^{-7}$ m^2 s^{-3}, $r_0 = 20$ km, $W = 10$ km, $f = 1.3 \times 10^{-4}$ s^{-1}, $N = 0.001$ s^{-1}, and $H = 2000$ m. The thick solid curve is the actual model shear. The dashed curve is the thermal wind shear based on the model density gradient according to (5). The thin solid curve is the estimated shear based on the one-dimensional, externally constrained response (33).

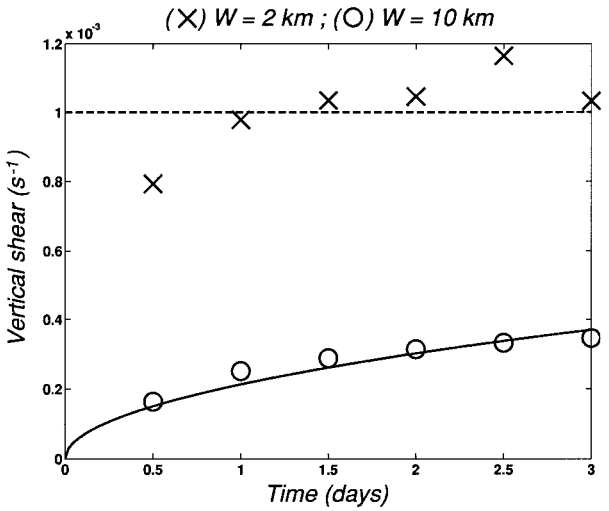

FIG. 11. Vertical shear at the surface in the center of the rim current ($r = r_0 + W/2$) vs time for deep convection with (circles) $W = 10$ km and (crosses) $W = 2$ km. Other parameters are $B_0 = 8 \times 10^{-7}$ m^2 s^{-3}, $r_0 = 20$ km, $f = 1.3 \times 10^{-4}$ s^{-1}, $N = 0.001$ s^{-1}, and $H = 2000$ m. The solid curve is the theoretical response for externally constrained convection given by (33). The dashed line is the theoretical response for internally constrained convection ($N = 0.001$ s^{-1}).

where (2) and (15) have been used. The vertical shear is fairly accurately estimated by the theoretical value within the central part of the rim current, supporting both the estimate of the density gradient and the importance of W. Near the edges of the rim current, lateral mixing smooths the sharp gradients predicted by the theory.

Additional confirmation of the importance of W comes from the time development of the vertical shear. Figure 11 shows the vertical shear at the surface at the center of the rim current versus time for two choices of W. According to (25) with $\alpha = 0.013$, the case of $W = 10$ km should be externally constrained with shear given by (33). The case of $W = 2$ km should be internally constrained with constant shear at the surface equal to N, according to (21). Of course, the shear in both cases must begin at zero because there is no initial density gradient. Therefore, the shear for $W = 2$ km requires about one day to reach the theoretical value, while the rim current adjusts toward geostrophy. The numerical results clearly follow the theoretical expectations after one day, despite exhibiting some scatter.

The transition from internally constrained to externally constrained convection can be viewed in terms of the surface vertical shear for a range of W (Fig. 12). Here, the model velocity shear and thermal wind shear at the surface at the center of the rim current are shown after 3 days, along with the theoretical estimates. For small W, the shears are close to the estimate of N for internally constrained convection. For large W, the shears approach the estimate for externally constrained convection (33). The theoretical transition, found by setting $t_d^* = 3$ days in (24), occurs at $W = 3.7$ km, in good agreement with Fig. 12.

Figure 13 shows the model velocity versus time for several choices of W, in the same manner as Fig. 4. For $W = 1$ km the response should be internally constrained, according to (25) with $\alpha = 0.013$, and should follow the square root curve given by (22), as it does. For

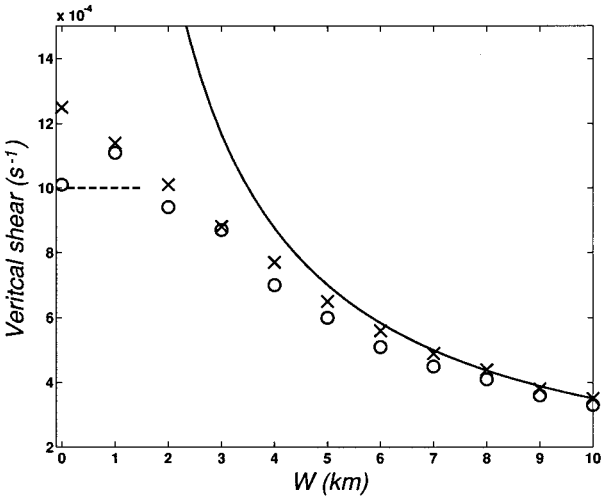

FIG. 12. Vertical shear at the surface in the center of the rim current ($r = r_0 + W/2$) after 3 days of deep convective forcing for various forcing decay widths W with $B_0 = 8 \times 10^{-7}$ m^2 s^{-3}, $r_0 = 20$ km, $f = 1.3 \times 10^{-4}$ s^{-1}, $N = 0.001$ s^{-1}, and $H = 2000$ m. Circles represent the actual model shear. Crosses represent the thermal wind shear based on the model density gradient according to (5). The solid curve is the estimated shear based on the one-dimensional, externally constrained response (33). The internally constrained response ($N = 0.001$ s^{-1}) is shown as a dashed line. The theoretical transition after 3 days occurs at $W = 3.7$ km, based on (24).

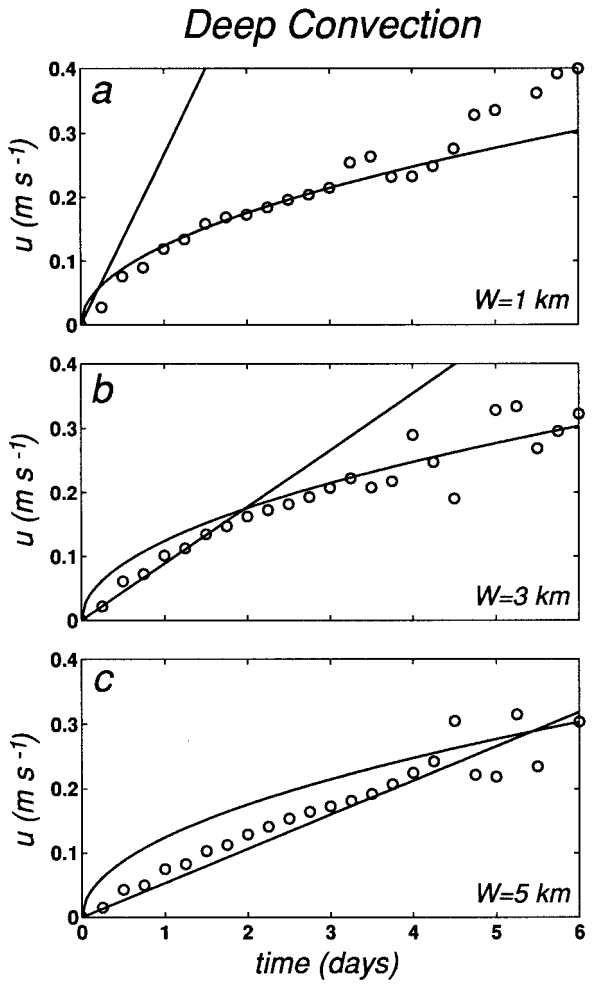

FIG. 13. Maximum cyclonic velocity at the surface within the rim current (open circles) vs time during deep convection with $B_0 = 8 \times 10^{-7}$ m^2 s^{-3}, $r_0 = 20$ km, $f = 1.3 \times 10^{-4}$ s^{-1}, $N = 0.001$ s^{-1}, $H = 2000$ m, and $W =$ (a) 1, (b) 3, and (c) 5 km. The straight line corresponds to the expected velocity for externally constrained convection given by (17), while the curve corresponds to the expected velocity for internally constrained convection given by (22). The intersection of the curves occurs at t_d^*.

$W = 3$ km, the model velocity initially follows the linear curve given by (17) and then switches to the square root dependence after t_d^*. For $W = 5$ km, the response should be externally constrained according to (25), and the model velocity follows the linear curve as expected. The good agreement between the model velocites and the estimates (17) and (22) again provides support for the theoretical ideas.

Finally, Fig. 14 shows the chimney density anomaly versus time for $1 \leq W \leq 10$ km, using the scalings (19) for externally constrained convection. The curves clearly tend to leave the one-dimensional response (dashed curve) near the same time as W increases, indicating that these scales are appropriate for larger W. There is more variability than found for shallow convection (Fig. 6), reflecting the more complex nature of the response. Nevertheless,

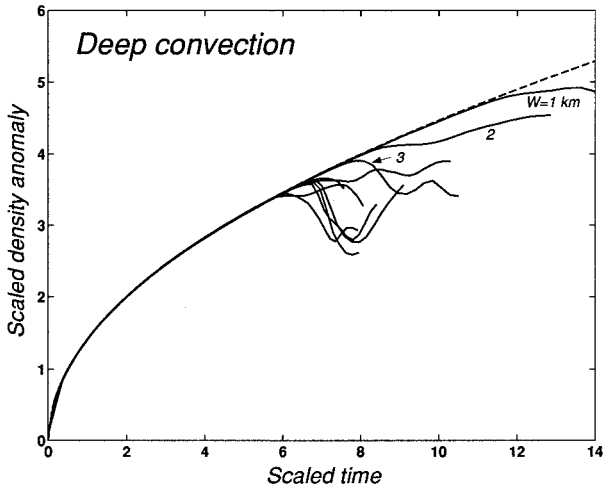

FIG. 14. Density anomaly within the forcing region vs time, with both axes scaled for deep, externally constrained convection using (18) and (19). Each curve represents the response for a different forcing decay width W from 1 to 10 km in unit increments. (Only a few of the curves are labeled to avoid confusion.) Other parameters are $B_0 = 8 \times 10^{-7}$ m^2 s^{-3}, $r_0 = 20$ km, $f = 1.3 \times 10^{-4}$ s^{-1}, $N = 0.001$ s^{-1}, and $H = 2000$ m.

the curves for $W \geq 4$ km all break away from the one-dimensional response near 3.5, consistent with Fig. 9a. This suggests that the estimate of $\alpha \approx 0.013$ is reasonable for externally constrained convection. For internally constrained convection, α can be estimated by equating the coefficient of ρ_{di} in (23) to the value of 3.9 found by VMJ, which produces $\alpha \approx 0.025$.

4. Discussion

The numerical results have largely confirmed the theoretical ideas presented in section 2 by demonstrating both the potential importance of the forcing decay width W and the smooth transition from internally constrained convection to externally constrained convection. All of the velocity scales and equilibrium scales are presented in Table 1 for comparison and easy reference. The results are perhaps slightly more convincing for shallow convection than for deep convection, but the behavior is robust enough in both cases to discuss some general implications.

The importance of the forcing decay region can be quantified by examining the transitions given by (14) and (25). These expressions have identical parameter dependencies, differing only in the coefficients. Remarkably, the estimates of α based on the numerical results produce coefficients that are within 15% of each other, so (14) and (25) are basically identical! Therefore, a single curve represents the transition between internally and externally constrained convection (i.e., both scales produce the same estimates at points on the curve) for all possible combinations of parameters (Fig. 15). This curve applies to both shallow and deep convection

TABLE 1. Formulas for baroclinic Rossby radius, rim current surface velocity, time to reach equilibrium, equilibrium density anomaly, equilibrium chimney depth, and eddy exchange efficiency α.

	Internally constrained	Externally constrained
	Shallow convection: $R_d = (\rho g H/\rho_0)^{1/2}/f = (B_0 t)^{1/2}/f$	
v_{si}, v_{se}	$\frac{1}{2}(B_0 t)^{1/2}$	$\frac{B_0}{2fW}t$
t_{si}, t_{se}	$\left(\frac{1}{\alpha}\right)^{2/3}\left(\frac{r_0^2}{B_0}\right)^{1/3}$	$\left(\frac{1}{\alpha}\right)^{1/2}\left(\frac{fr_0W}{B_0}\right)^{1/2}$
ρ_{si}, ρ_{se}	$\left(\frac{1}{\alpha}\right)^{2/3}\frac{\rho_0}{gH}(B_0 r_0)^{2/3}$	$\left(\frac{1}{\alpha}\right)^{1/2}\frac{\rho_0}{gH}(fB_0 r_0 W)^{1/2}$
α	0.044	0.031
	Deep convection: $R_d = Nh/f = (2B_0 t)^{1/2}/f$	
v_{di}, v_{de}	$\frac{\sqrt{2}}{3}(B_0 t)^{1/2}$	$\frac{B_0}{2fW}t$
t_{di}, t_{de}	$\frac{1}{2}\left(\frac{3}{2\alpha}\right)^{2/3}\left(\frac{r_0^2}{B_0}\right)^{1/3}$	$\left(\frac{1}{2\alpha}\right)^{1/2}\left(\frac{fr_0W}{B_0}\right)^{1/2}$
ρ_{di}, ρ_{de}	$\left(\frac{3}{2\alpha}\right)^{1/3}\frac{\rho_0 N}{g}(B_0 r_0)^{1/3}$	$\left(\frac{2}{\alpha}\right)^{1/4}\frac{\rho_0 N}{g}(fB_0 r_0 W)^{1/4}$
h_{di}, h_{de}	$\left(\frac{3}{2\alpha}\right)^{1/3}\frac{1}{N}(B_0 r_0)^{1/3}$	$\left(\frac{2}{\alpha}\right)^{1/4}\frac{1}{N}(fB_0 r_0 W)^{1/4}$
α	0.025	0.013

and for all scales, from the laboratory to the ocean. It is also independent of stratification and total depth. Parameter combinations that lie below the curve produce internally constrained convection with scales set by the baroclinic Rossby radius. The VMJ scales apply: (12) for shallow convection or (23) for deep convection. Parameter combinations that lie above the curve produce externally constrained convection with W setting the scales. The CG scales apply: (9) and (10) for shallow convection or (18) and (19) for deep convection. The dashed curves represent a 25% difference between the equilibrium time predictions of the VMJ and CG scales.

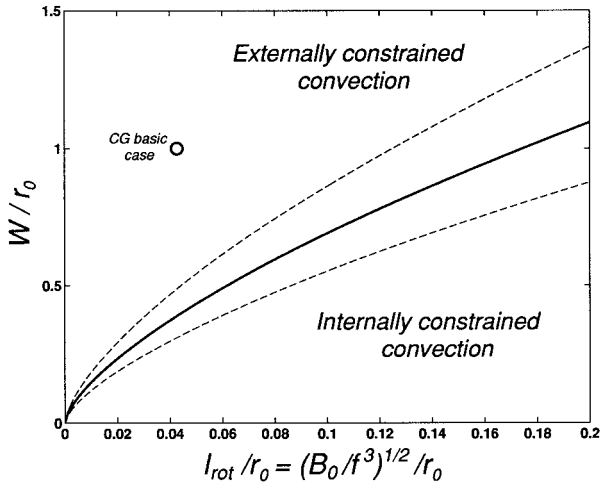

FIG. 15. Solid curve is the transition between internally and externally constrained convection given by (14) with $\alpha = 0.031$. Dashed curves represent a 25% difference between the equilibrium time predictions of the VMJ and CG scales. This plot applies to both shallow and deep convection because the coefficients of (14) and (25) are almost the same. The open circle represents the basic case considered by CG.

The open circle in Fig. 15 represents the standard case of CG ($B_0 = 4 \times 10^{-7}$ m^2 s^{-3}, $f = 1.3 \times 10^{-4}$ s^{-1}, $r_0 = 10$ km, $W = 10$ km), which lies well above the transition curve, so the convection is externally constrained. This explains their good agreement with scales (9) and (10). Even the strongest buoyancy flux that CG considered ($B_0 = 16 \times 10^{-7}$ m^2 s^{-3}) lies in the externally constrained region, well above the transition. Of course, all other numerical and laboratory models have used $W = 0$, placing them below the transition curve, in the internally constrained region. Figure 15 may then be used to estimate how large W would need to be, relative to r_0, to move above the curve. For example, VMJ considered $B_0 = 3.9 \times 10^{-7}$ m^2 s^{-3}, $f = 10^{-4}$ s^{-1}, $r_0 = 8$ km (their Fig. 6) for which $l_{rot}/r_0 = 0.078$. The transition occurs at $W/r_0 = 0.58$, so a forcing decay width of $W > 4.65$ km would change the response to externally constrained convection. Another example from VMJ is $B_0 = 8 \times 10^{-7}$ m^2 s^{-3}, $f = 10^{-4}$ s^{-1}, $r_0 = 40$ km (their Fig. 3) for which $l_{rot}/r_0 = 0.022$. From Fig. 15, the transition occurs at $W/r_0 = 0.25$, so $W > 10$ km would lead to externally constrained convection. Thus, for these examples, the forcing decay scale need not be terribly large to change the scaling.

Laboratory models cover a wide range of parameters, from small l_{rot}/r_0 comparable to numerical models to larger values that approach $l_{rot}/r_0 = O(1)$. For example, Brickman (1995) reports cases that correspond to the

range 0.0064 to 0.693; Coates et al. (1995) from 0.015 to 0.11; Maxworthy and Narimousa (1994) from 0.002 to 0.4; and Whitehead et al. (1996) from 0.1 to 0.83. The cases involving small values of l_{rot}/r_0 require relatively narrow forcing decay regions to become externally constrained. However, for larger values of l_{rot}/r_0, Fig. 15 shows that a forcing decay region as wide or wider than r_0 would be required to change from internally constrained to externally constrained convection ($W/r_0 \geq 1$). So, laboratory tests of the ideas presented here should probably concentrate on cases with small l_{rot}/r_0 because large W may present additional technical difficulties (to say nothing of the difficulty in producing a well-behaved forcing decay region in the lab).

In general, Fig. 15 shows that, for weak buoyancy fluxes and/or large convecting regions ($l_{rot}/r_0 \ll 1$), the forcing decay width need only be a small fraction of the forcing region to set the scales. For strong buoyancy fluxes and/or small convecting regions ($l_{rot}/r_0 \geq 0.2$), the forcing decay width must be a substantial fraction of the forcing region to set the scales. Thus, smaller forcing regions are more likely to produce internally constrained convection, while larger forcing regions are more likely to produce externally constrained convection.

Typical ocean values result in small l_{rot}/r_0. For example, ocean buoyancy fluxes over Arctic shelves tend to be in the range of $B_0 \approx 2$–4 ($\times 10^{-7}$ m^2 s^{-3}) with occasional values as high as 8×10^{-7} m^2 s^{-3} (e.g., Cavalieri and Martin 1994). Convecting regions have a radius of about 10–20 km (e.g., Pease 1987). Taking $f = 1.3 \times 10^{-4}$ s^{-1} yields $0.01 \leq l_{rot}/r_0 \leq 0.04$. Figure 15 suggests that W need only be a small fraction of r_0 (i.e., a fews kilometers) to produce externally constrained convection. Atmospheric scales of variability associated with cooling regions are likely to be much larger than a few kilometers. Scales of variability associated with salt fluxes accompanying ice formation, though not well established, are probably at least several kilometers. Therefore, accurate predictions of properties of dense water formed during ocean convection may require knowledge of the spatial scales over which the buoyancy forcing varies, and not only the average buoyancy flux over the forcing region.

It is tempting to draw conclusions about the efficiency of eddy exchange based on the estimates of α in Table 1, but this must be done with caution because α has been defined in different ways in this and previous works. For example, it was pointed out following the derivation of both (12) and (23) that the present definition of α differs from that of VMJ. In fact, CG compared their estimate for shallow, externally contrained convection in a semielliptical coastal polynya (0.043) directly to the VMJ estimate for deep, internally constrained convection using the VMJ definition (0.008) and concluded that they differ by a factor of 5. However, as was pointed out following (23), the VMJ estimate consistent with the development presented here and in CG is a factor of 3 larger (0.025). So, the conclusion made by CG is incorrect.

Furthermore, Spall and Chapman (1997, submitted to *J. Phys. Oceanogr.*) have recently proposed a theory for calculating α from first principles. They consider only narrow fronts (i.e., internally constrained convection) and find that their efficiency coefficient, which they call c_e, should be constant, independent of externally imposed parameters. Their predicted value is $c_e = 0.045$, while their numerical calculations produce somewhat smaller values of $c_e = 0.02$–0.04. The present estimate for shallow, internally constrained convection is close to the theoretical value, but again caution is needed. The velocity scale used in the theory of Spall and Chapman is the total vertical change in geostrophic velocity in the rim current, rather than the surface velocity used here. For deep convection, these are almost the same. For shallow convection, they differ by a factor of 2, which would reduce the present estimate to $c_e = 0.022$, which is then in the range of values found numerically by Spall and Chapman and nearly equal to the value for deep convection (0.025). Likewise, the value found by CG should be reduced by a factor of 2, producing $c_e = 0.021$ which is again in the range obtained by Spall and Chapman. Interestingly, the equivalent estimate of c_e for shallow, externally constrained convection would be 0.015, almost the same as the estimate for deep, externally constrained convection. So, c_e appears to be constant for externally constrained convection as well. The point is that all of these calculations produce estimates of the eddy exchange efficiency that are comparable when using a standard derivation. One might argue, perhaps, that externally constrained convection may be somewhat less efficient at cross-frontal exchange than internally constrained convection, but this is speculative given the range of estimates and the lack of reasons for such a difference.

Finally, some caveats are in order. The calculations presented here were designed specifically to examine the transition between internally and externally constrained convection and, thereby, to reconcile the two sets of scales derived by VMJ and CG. Thus, with few exceptions, the forcing decay width W was varied while the other parameters were held fixed. The results of VMJ and CG provide enough support for the generality of the response, so other parameter variations were deemed unnecessary. In addition, the scenarios are highly idealized, neglecting many factors that may (and probably do) play important roles in the ocean. For example, a depth of $H = 50$ m was chosen for the shallow convection calculations to ensure that the convection reached the bottom rapidly so that a hydrostatic model would be appropriate. Clearly, wind forcing could considerably alter the flow beneath the forcing region. Likewise, time variability in the buoyancy forcing, probably leading to spatial variability, could also change the response markedly, as could ambient currents and bottom topography. All of these features deserve con-

sideration in future studies but are beyond the purpose of this study.

5. Conclusions

The ocean response to negative buoyancy flux, applied in an isolated region at the surface, has been investigated using the approach of VMJ, to determine the scales of the equilibrium state, that is, the time to reach equilibrium, the equilibrium density anomaly within the convecting chimney, and, in the case of deep convection, the equilibrium depth of the chimney. Two types of isolated convection have been distinguished based on the importance of the forcing decay region surrounding the buoyancy forcing region and across which the buoyancy flux decreases to zero. A narrow forcing decay region produces internally constrained convection in which the baroclinic Rossby radius is the dominant horizontal length scale, and the resulting equilibrium scales are those found by VMJ. A wide forcing decay region produces externally constrained convection in which the forcing decay width is the dominant horizontal length scale, and the equilibrium scales are those found by CG.

The transition between the two types of convection is smooth and approximately given by (14) for shallow convection and (25) for deep convection. These equations are identical for practical purposes, so a single curve (Fig. 15) captures the essence of all possible combinations of buoyancy flux, rotation rate, forcing region radius, and forcing decay width. Surprisingly, the transition is independent of the total depth and the ambient stratification for both shallow and deep convection.

The results suggest that weak buoyancy fluxes and/or large convecting regions ($l_{\text{rot}}/r_0 \ll 1$) require a relatively narrow forcing decay width to produce externally constrained convection, whereas strong buoyancy fluxes and/or small convecting regions ($l_{\text{rot}}/r_0 \geq 0.2$) require a relatively wide forcing decay width to produce externally constrained convection. The forcing decay region need not be terribly wide to be important in typical ocean convection situations, especially for large forcing regions.

Acknowledgments. I thank Glen Gawarkiewicz and Steve Lentz for numerous enlightening discussions and helpful suggestions during the course of this research. I am grateful for the financial support provided by the National Science Foundation (NSF) as part of the Arctic Systems Science (ARCSS) program, which is administered through the Office of Polar Programs (Grant OPP-9422292). The numerical calculations reported here were performed at the National Center for Atmospheric Research (NCAR) in Boulder, Colorado, which is funded by NSF.

APPENDIX

Accounting for the Entire Buoyancy Flux

The buoyancy flux within the forcing decay region is ignored to derive (3) and the subsequent theoretical expressions in section 2. The error introduced by this assumption is small, even when W is the same size as r_0. To demonstrate, I use the entire area of imposed buoyancy forcing to evaluate (1), that is, $0 < r \leq r_0 + W$ with B given by (2). In this case, (3) becomes

$$\left(\frac{1}{2\alpha}\right)\frac{\rho_0}{g}B_0 r_0 \epsilon = \upsilon\rho h, \tag{A1}$$

where

$$\epsilon = 1 + \frac{1}{3}\frac{(W/r_0)^2}{(1 + W/r_0)}.$$

The additional buoyancy flux within the forcing decay region is included in the factor ϵ. Subsequent equations then require that r_0 be replaced by $r_0\epsilon$. However, the maximum ϵ for the calculations presented here is 1.06 (for $r_0 = 20$ km and $W = 10$ km), and ϵ only varies from 1 to 1.17 for $0 \leq W/r_0 \leq 1$. Therefore, these small errors are ignored in order to simplify the theory of section 2.

REFERENCES

Alverson, K. D., 1995: Topographic preconditioning of open ocean deep convection. Ph.D. thesis, MIT/WHOI, 95-26, 146 pp. [Available from Woods Hole Oceanographic Institution, Woods Hole, MA 02543.]

Brickman, D., 1995: Heat flux partitioning in open-ocean convection. *J. Phys. Oceanogr.,* **25,** 2609–2623.

Cavalieri, D. J., and S. Martin, 1994: The contributions of Alaskan, Siberian, and Canadian coastal polynyas to the cold halocline layer of the Arctic Ocean. *J. Geophys. Res.,* **99,** 18 343–18 362.

Chapman, D. C., and G. Gawarkiewicz, 1997: Shallow convection and buoyancy equilibration in an idealized coastal polynya. *J. Phys. Oceanogr.,* **27,** 555–566.

Coates, M. J., G. N. Ivey, and J. R. Taylor, 1995: Unsteady, turbulent convection into a rotating, linearly stratified fluid: Modeling deep ocean convection. *J. Phys. Oceanogr.,* **25,** 3032–3050.

Gawarkiewicz, G., and D. C. Chapman, 1995: A numerical study of dense water formation and transport on a shallow, sloping continental shelf. *J. Geophys. Res.,* **100,** 4489–4507.

Haidvogel, D., J. Wilkin, and R. Young, 1991: A semi-spectral primitive equation ocean circulation model using vertical sigma and orthogonal curvilinear horizontal coordinates. *J. Comput. Phys.,* **94,** 151–185.

Jones, H., and J. Marshall, 1993: Convection with rotation in a neutral ocean: A study of open-ocean deep convection. *J. Phys. Oceanogr.,* **23,** 1009–1039.

——, and ——, 1997: Restratification after deep convection. *J. Phys. Oceanogr.,* **27,** 2276–2287.

Maxworthy, T., and S. Narimousa, 1994: Unsteady, turbulent convection into a homogeneous, rotating fluid, with oceanographic applications. *J. Phys. Oceanogr.,* **24,** 865–887.

Pease, C. H., 1987: The size of wind-driven coastal polynyas. *J. Geophys. Res.,* **92,** 7049–7059.

Spall, M. A., and D. C. Chapman, 1997: On the efficiency of baroclinic eddy heat transport across narrow fronts. *J. Phys. Oceanogr.,* submitted.

Visbeck, M., J. Marshall, and H. Jones, 1996: Dynamics of isolated convective regions in the ocean. *J. Phys. Oceanogr.,* **26,** 1721–1734.

Whitehead, J. A., J. Marshall, and G. Hufford, 1996: Localized convection in rotating stratified fluid. *J. Geophys. Res.,* **101,** 25 705–25 722.